Research article

Studying the redistribution of kinetic energy between the morphologically distinct parts of the fragments cloud formed from high-velocity impact fragmentation of an aluminum sphere on a steel mesh

Nikolay Myagkov* and Timofey Shumikhin

Institute of Applied Mechanics, Russian Academy of Sciences, 125040, Moscow, Russia

* Correspondence: Email: nn_myagkov@mail.ru; Tel: +74959461765.

Abstract: Numerical simulations of experiments (Shumikhin et al., 2014) on the fragmentation of aluminum spheres with diameter of 6.35 mm on single steel-mesh bumpers of different specific mass are carried out in the present work. Specific mass of the mesh bumpers in these experiments was varied by changing the diameter of the wire from which was woven the mesh. The spatial distribution of fragments, their mass and kinetic energy (KE) are determined. The results of the numerical simulations are in good agreement with the experimental data showing that the cloud of fragments composes of two morphologically distinct groups of fragments, which differ greatly in mass: the central group, consisting mainly of four large fragments, and four groups of linearly-distributed chains of smaller fragments. The numerical simulations in agreement with the experiments show that KE of the central group of fragments decreases relative to the total KE of the fragments cloud with increasing the specific mass of the mesh, while the relative KE of other smaller fragments increases.

1. Introduction

The fragmentation of a solid, caused by its interaction with a thin shield at high velocities of

impact, has been the subject of researches for quite a long time. These researches are carried out mainly in the framework of work aimed at improving the shield protection of spacecraft from the impacts of space debris and meteoroids [1]. Important place in these studies is occupied by a mesh which allows one to reduce the total weight of the composite shield of the spacecraft protection while maintaining its effectiveness [2–4]. The effectiveness of the composite shields with meshes has sparked interest in the study of the fragmentation properties of single mesh bumper. Studies of the projectile fragmentation on the mesh bumpers have been conducted since the 1990s (e.g., [5–10]). In the papers [5,10], the comparative study of high-velocity projectile fragmentation on mesh and continuous bumpers was carried out, and the fragmentation and dispersive properties of a mesh or a stack of meshes during their interaction with projectile were considered. In these papers, it was shown that the fragmentation of the projectile on the mesh bumper formed a cloud of fragments that produce crater groups linearly distributed over the surface of the witness plate.

The shield protection systems made of steel meshes and aluminum plates were installed in some zones of ISS module FGB "Zarya" [11]. Moreover, some similar prototypes were implemented in the frame of preparation for the launch of a new ISS module MLM. The advantage of the use of steel meshes in actual micro-meteoroid and orbital debris shielding protection motivated a series of studies aimed at finding of possible further options for optimization of the low-weight shielding design [12,13]. Experiments [12,13] were performed to comply with the requirements similar to those used in the course of preliminary work on ISS modules shielding. They revealed that there are a number of lighter assemblies that can withstand an impact of an aluminum projectile with diameter 6.35 mm in the range of velocities from 2.5 to 3.5 km/s. The total areal density of those assemblies including the weight of the protected wall was in the range from 12.71 to 17.34 kg/m^2. These assemblies were fabricated of relatively lighter steel meshes made of wires with diameters from 0.25 to 0.40 mm and with mesh openings from 1.0 to 2.5 mm. Meanwhile, the other series of tests [9] were performed with heavier single steel meshes made of wire of diameters from 0.6 to 1.2 mm with mesh opening 2 mm. The impact of an aluminum 6.35 mm projectile into these meshes revealed a useful effect consisted in the fact that the fragmentation of the projectile resulted in formation of four large fragments instead of a single largest one as it usually took place with continuous bumpers. The other substantial part of the fragments cloud was four jets of particles emitted from the projectile. An important aspect concerning the formation of the four large fragments was the fact that under condition of deep vacuum these fragments had no tendency for lateral splitting and acted on a second bumper like an intact largest fragment or a dense group of fragments [6] which increased the risk of perforation. The splitting of the fragments was observed at lower degree of vacuumization or at normal atmospheric pressure. The higher separation of the largest fragments into four large ones is a positive factor since it results in less degree of localization of terminal impact pulse. To provide the splitting of the large fragments in the deep vacuum a low-density block of polystyrene was used in [6]. The block of the 80 mm height made of polystyrene foam was installed on the path of the fragments cloud generated at an impact of 6.35 mm aluminum projectile on a single steel mesh made of 0.6 mm wire with mesh opening 2.0 mm. The total weight of all assembly including the rear wall was 12.63 kg/s. This combination of the heavier mesh and polystyrene foam provided non-perforation by a 6.35 mm aluminum projectile at velocity 3.47 km/s [6]. The character of damage on the non-perforated second bumper witnessed that this scheme could provide some additional reserve of resistance. The damages of the rear wall consisted of the craters produced only by the large fragments. The action of the jets was completely absorbed by polystyrene foam block. This result

motivated the further study of the fragments cloud generated at impact on heavier meshes [9]. The idea was to understand how the kinetic energy of the fragments cloud is distributed among its different parts so the mesh parameters and foam block thickness could be optimized for lower weight with better performance.

Numerical simulations of the experiments in [9] are carried out in the present work. The parameters of the experiments [9] are presented in Table 1. A 6.35 mm-diameter aluminum-alloy (Al 2017) sphere was used as a projectile. One can see (Table 1) that specific mass of the steel mesh bumpers in the experiments was varied by changing the diameter of the wire from which was woven the mesh. The projectile velocity ranged from 3.20 to 3.40 km/s (Table 1). The scheme of the experiments is shown in Figure 1. The projectiles were accelerated using the two-stage light-gas (hydrogen) gun. The projectile velocities were measured by contactless laser sensors. The 15 mm thick witness plate made of D16 aluminum alloy was installed at a distance of 150 mm from the examined bumper. Fragmentation was analyzed by studying the morphology of damages to the surface of the witness plate. The crater volumes on the witness plates were measured. This series of experiments was made without vacuumization of the ballistic path at normal barometric pressure. The effect of air resistance had obviously a positive effect, since the movement of the fragments cloud through the air the aerodynamics forces contributed in higher separation of larger fragments providing more distinct imprint on the witness plate.

Table 1. Data of the experiments.

№ experiment	Impact velocity, (km/s)	Mesh parameters[*)] $l_a \times d_w$, (mm $\times$ mm)	The specific mass of the mesh bumper, (kg/m^2)
1	3.40	2.00 $\times$ 0.60	1.71
2	3.35	2.00 $\times$ 0.60	1.71
3	3.35	2.00 $\times$ 0.60	1.71
4	3.25	1.80 $\times$ 0.70	2.33
5	3.20	2.00 $\times$ 1.00	3.83
6	3.37	2.00 $\times$ 1.00	3.83
7	3.36	2.00 $\times$ 1.00	3.83
8	3.31	2.00 $\times$ 1.20	5.24

[*)] d_w is the wire diameter and l_a is the aperture (inside light visible distance between adjacent wires).
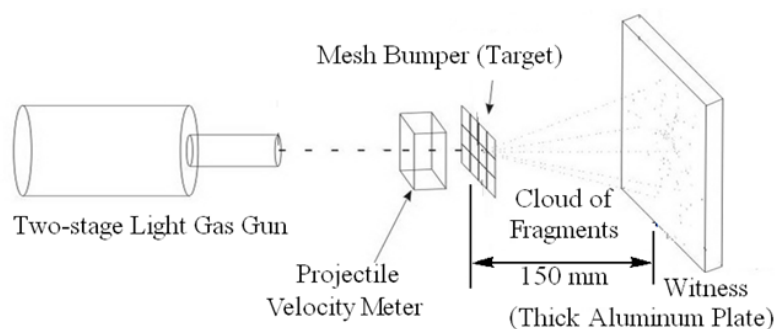

Figure 1. Scheme of the experiments with mesh bumpers.

Figure 2 shows the photo of a projectile and a mesh, and Figure 3 shows the typical features of the morphology of damages of the witness plate in experiments with the mesh bumper.

The impact on the witness-plate of the projectile fragments made it possible to fix their spatial distribution and kinetic energy, since in the range of velocities under consideration the volume of a crater produced by a fast-flying compact object is linearly proportional to its kinetic energy. The latter is a rule well known in ballistics [14]. Thus, by estimating the volumes of all craters, it is possible to estimate the kinetic energy distribution between the fragments or groups of fragments. Figure 4 shows the scheme of crater volume measurements in the experiments [9]. The volume of the crater was approximated by half the volume of the ellipsoid constructed by rotating around the major or minor axis of the ellipse defined from the contour of this crater on the surface of the witness-plate. Besides, the volumes of larger craters were additionally estimated by filling the craters with fine sand with subsequent weighting on a sensitive electronic balance.

It emerged [9,10] that when the projectile diameter to mesh cell size ratio fell in the range 2.1–2.5, the projectile fragmentation led to the formation of a group with four large craters and four crosswise groups of linear-distributed craters (Figure 3). The crater size in each chain group grows with moving away from the centre (i.e., from the shot-line/witness-plate intersection point). In addition, the witness-plate is no damage that could correspond to the biggest central fragment of the projectile. The absence of the central fragment would be non-relevant for the case of fragmentation of an aluminum projectile having the same diameter and velocity on a continuous bumper of equal specific mass.
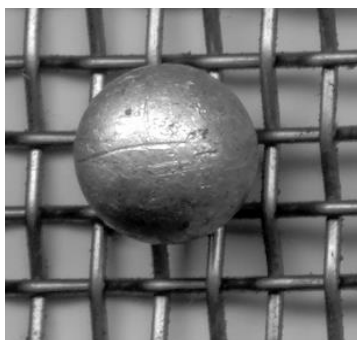

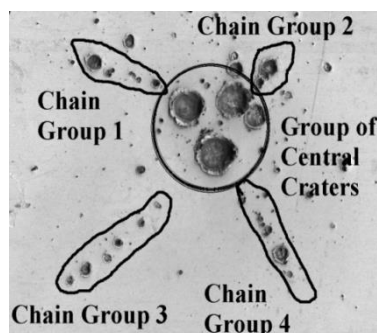**Figure 2.** Photo of projectile and mesh bumper.

Figure 3. Typical features of the morphology of damages of the witness plate in experiments with mesh bumper (experiment 4 from Table 1).
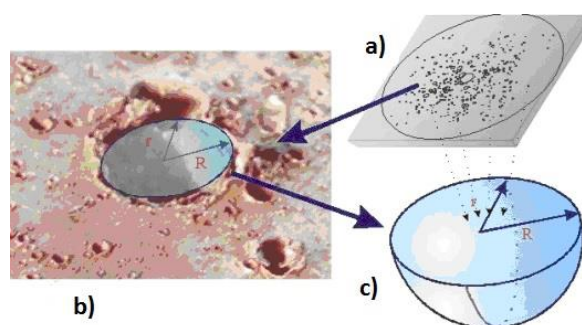
Figure 4. The scheme of recovery of the crater volume along its contour: (a) witness-plate, (b) a crater on the witness plate with an ellipse approximating its contour on the surface, and (c) a semi-ellipsoid built along the semi-axis of the ellipse.

To simulate the experiments presented in Table 1, a series of numerical calculations was performed in which the mass and kinetic energy (KE) of the projectile fragments formed after its interaction with the mesh were calculated in this paper.

2. Numerical simulation method and material model

Numerical simulations in 3D geometry were based on the system of equations of deformed solid mechanics and performed using the SPH method implemented in LS-DYNA Version 971 program package [15]. The lack of a grid allows SPH to model the problems that are difficult to solve by other methods, including fragmentation process and motion of the fragments cloud. An exhaustive review of SPH theory and application can be found, for example, in [16].

The material model is similar to that which we used in the paper [17]. The Prandtl–Reuss flow rule with the von Mises yield condition was used to describe the regime of plastic flow [15]. The constitutive equations of the problem under consideration were the Mi-Gruineisen equation of state [18] and the Johnson–Cook model [19] for the yield strength. The aluminum alloy and steel data that we used in the simulations are shown in Table 2, where are denoted: ρ_0 is the initial density of the material; K is the bulk modulus; G is the shear modulus; σ_p is the tensile strength; k is the factor of the shock adiabat $D = c_0 + k*U$; Γ is the Gruneisen coefficient, which is assumed to be constant. The values σ_p correspond to the spall strength measurements [20] for the aluminum alloy AMG6 and the steel St.3.

Table 2. Material parameters.

Material	ρ_0, g/cm^3	K, GPa	G, GPa	σ_p, GPa	$k*$	Γ
Aluminum alloy	2.71	72.8	27.3	1.15	1.34	2.0
Steel	7.85	166.7	76.9	1.66	1.49	1.93

In the Johnson–Cook model [19], the yield strength has the form:

$$Y = \left(A + B(\bar{\varepsilon}^{p})^{n}\right) \cdot (1 + C \ln \dot{\varepsilon}^{*}) \cdot \left(1 - (T^{*})^{m}\right) \tag{1}$$

where $\bar{\varepsilon}^p$ is the effective plastic strain; $\dot{\varepsilon}^* = \dot{\bar{\varepsilon}}^p/\dot{\varepsilon}_0$ is the effective plastic strain rate; $\dot{\varepsilon}_0 = 1 \text{ sec}^{-1}$; $T^* = (T - T_0)/(T_m - T_0)$, where T_0 and T_m is the initial and melting temperature, respectively. Parameters A, B, C, n, m and T_m in Eq 1 are the material parameters. Their values used in the simulations are presented in Table 3.

Table 3. Parameters for the Eq 1.

Material	ρ_0, g/cm^3	Heat capacity, kJ/(kg·K)	A, MPa	B, MPa	C	n	m	T_m, K	T_0, K
Steel	7.85	0.477	792	510	0.014	0.26	1.03	1793	293
Aluminum alloy	2.71	0.875	337	343	0.01	0.41	1.0	875	293

An important characteristic in search of fragments is the radius of influence r_{inf} which means the maximum distance at which two SPH particles are still belonging to the same fragment. Following [17], the radius of influence in the present simulations was selected to be $r_{inf} = a\sqrt{3}$, where a is the cubic lattice constant in the initial disposition of the SPH particles. In all simulations, the calculations were performed up to the point in time when the distribution of fragments by mass could be treated as stationary. Depending on the number of the SPH particles in the projectile, this time was $t_{st} = 50–80$ μs after the impact. The 3D coordinates of all SPH particles for the time t_{st} were initial data for the search of fragments.

The simulations were carried out for the spherical aluminum-alloy projectiles with the 6.35 mm diameter impacting with velocity 3.0 km/s and the steel meshes with wire diameter $d_w = 0.6–1.2$ mm (Table 4). In all calculations, the projectile motion line was perpendicular to mesh bumper and was aimed at the node (intersection of wires) located in the center of the mesh bumper. The number of SPH particles which we used in simulations for different projectile-mesh combinations are presented in Table 4.

Table 4. Initial data of the numerical simulations.

№	The mesh parameters, $l_a \times d_w$, (mm × mm)	The number of SPH particles in the projectile	The number of SPH particles in the mesh bumper	The specific mass of the mesh bumper, (kg/m^2)
(i)	2.0 × 0.60	17269	10710	1.71
(ii)	2.0 × 0.80	33641	33222	2.82
(iii)	2.0 × 1.00	47257	72002	4.11
(iv)	2.0 × 1.20	27369	61642	5.55

The results of the simulations were averaged over an ensemble (i.e., no less than 10) of simulations corresponding to the same value of the impact velocity V. The simulations corresponding to the same impact velocity V differed from one another due to perturbation introduced in the initial conditions (the initial angular displacement of the projectile relative to its rotation axis).

3. Results

Picture of the witness-plate damage in the experiment 5 (Table 1) is shown in Figure 5a. In the geometric center of all damages, there is a group of four large craters (in this case, a thin plate of an aluminum witness was placed on a thick aluminum substrate and it can be seen that the impacts of the four largest fragments formed holes in the plate). Figure 5b depicts the fragments cloud obtained in numerical simulation performed with close initial parameters (iii in Table 4). The four largest fragments are located similar to the holes on the witness in Figure 5a. The elongated clouds of smaller fragments diverge from these large fragments. The distribution of fragments in the 3D space is shown in Figure 5c. The four largest fragments are formed from the back of the projectile, as can be seen from their location in the body of the spherical projectile before impact contact with the bumper (Figure 5d). Thus, it can be seen from Figure 5 that numerical calculations are in good agreement with experiment, showing that the cloud of fragments consists of two morphologically different groups of fragments: a central group consisting of four large fragments, and a cross-like arrangement of four groups of linearly distributed chains of smaller fragments.
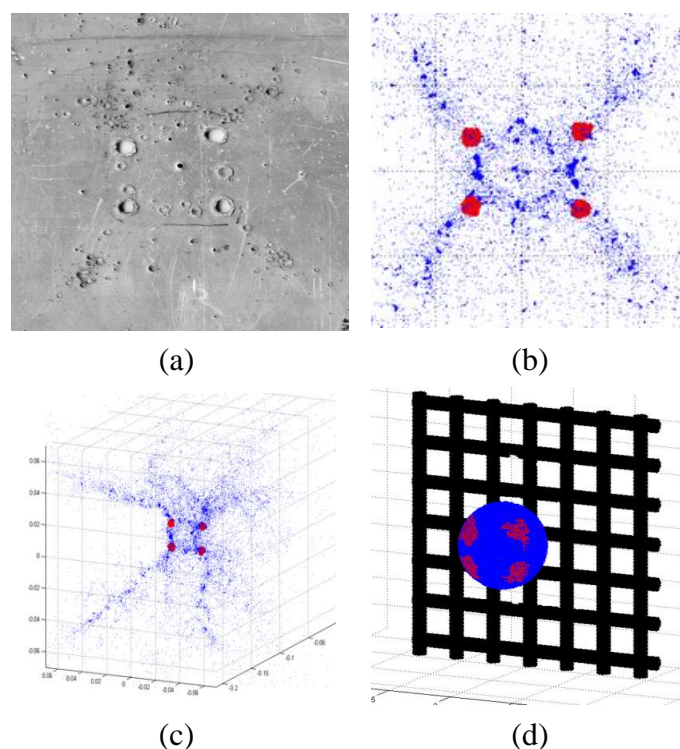

(a) (b)

(c) (d)

Figure 5. (a) Experiment 5 of Table 1 with the mesh of 2.0 mm × 1.0 mm. (b) Simulation (iii in Table 4) with the mesh of 2.0 mm × 1.0 mm. (c) The fragments distribution of in 3-dimensional space. (d) The location of the four largest fragments in the back of the projectile before its impact contact with the mesh.

Figure 6 shows the dependence of kinetic energy (KE) of fragments on their mass for all four variants of calculation from Table 4, corresponding to meshes with wire diameters of 0.6 mm, 0.8 mm, 1.0 mm and 1.2 mm. From Figure 6, it can be seen that:

(1) In all variants of calculations, the largest fragment has the largest KE.

(2) In all variants of calculations, all fragments are divided into two groups with a substantially different average mass of fragments in groups.

(3) In each group of large fragments (the so-called central group), there are 4 fragments.

The last two points from the above are in good agreement with the experiment, showing as already noted above that the cloud of fragments consists of two morphologically distinct groups of fragments. The result of the simulations showing that the largest fragment has the largest KE is important, since it cannot be obtained directly from experiments where the witness-plate is used as a recorder of fragments.
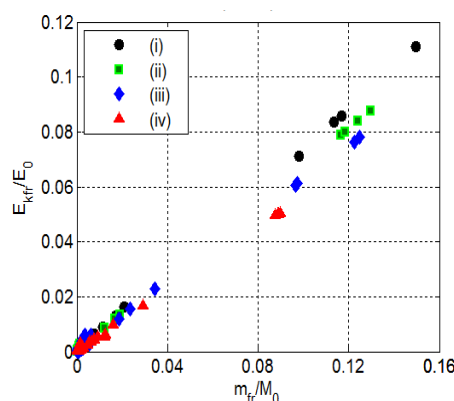

Figure 6. The dependence of KE of fragments on their mass normalized to the initial mass (M_0) and KE (E_0) of the projectile for the four variants of the initial parameters from Table 4.

Figures 7a and 8a give a graphical representation of the experimental data [9] (Table 1) in the form of the dependence of the crater volumes on the wire diameter of the mesh. Taking into account, the fact that the crater volume is proportional to the KE of the fragment that formed it, the presented graphs reflect the distribution of KEs between different parts of the cloud of fragments that correspond to morphologically distinct groups of craters. Figures 7b and 8b show the results of calculations (Table 4) in the form of the dependence of KE of fragments (normalized to the initial KE of the projectile), on the diameter of the wire. It can be seen that the results of the simulations agree qualitatively with the results of the experiments.

The behavior of the KE of the entire cloud of fragments is reflected in curve 1 (Figure 7a,b). It is seen that it decreases with increasing specific mass of the mesh. The reduction of KE fragments can be associated with an increase in the work of plastic deformation and the work of destruction of the projectile and the bumper. The increase in the specific mass of the mesh bumper, as in the case of continuous bumpers, leads to a more intensive deforming and crushing of the projectile, which means an increase in the work of plastic deformation and destruction. The KE dependence of fragments of the central group also has a decreasing character. Apparently, the fragments forming the central group of craters are an analog of the so-called central leader, i.e., one large fragment located in the front central part of the fragments cloud when the projectile is destructed on continuous bumper [21]. The size and KE of the central leader decreases with increasing thickness of the continuous bumper due to the spalling mechanism of the projectile destruction, as a result of which sufficiently small fragments are separated from the rear side of the projectile—the longer the impact

pulse (which is proportional to the thickness of the bumper), the greater the projectile-mass loss and the less the residual central leader. In our case of the mesh bumper, the KE of the largest fragment (Figure 7a,b) does not have an obvious tendency to decrease with increasing specific mass of the bumper.

The normalized data (Figure 8) show that the relative KE of the central group of fragments decreases relative to the total KE of the fragments cloud with increasing the wire diameter (specific mass) of the mesh, while the relative KE of other smaller fragments increases. With regard to the shielding protection of spacecraft from meteoroids and orbital debris clouds, this means a redistribution of KE of fragments over a larger area of the protecting wall, reducing the probability of it perforation.
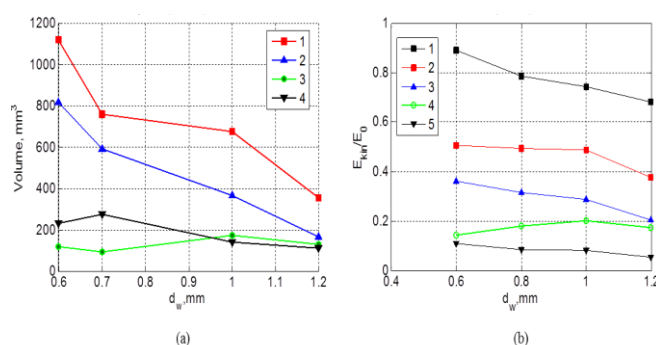

Figure 7. (a) The experimental data as the dependences of the craters volume on the wire diameter. Legend: 1: volume of all damage; 2: volume of craters in the central group; 3: volume of linearly distributed craters; 4: volume of the largest crater on the witness. (b) The simulation results as the dependences of the KE on the wire diameter normalized to the initial KE (E_0) of the projectile. Legend: 1: complete KE of the fragments cloud; 2: KE of the fragments cloud containing 2 or more SPH particles; 3: KE of the central group of the fragments; 4: KE of the group of smaller fragments obtained as a difference between curves 2 and 3; 5: KE of largest fragment.
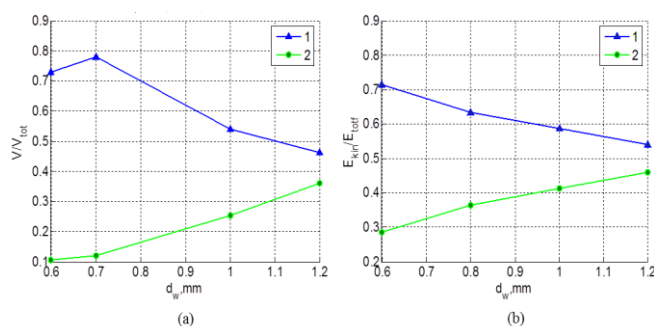

Figure 8. (a) The experimental data in the form of crater volumes of central (1) and linearly distributed (2) groups normalized to the volume of all craters, depending on the wire diameter. (b) The simulation results in the form of the KE of the central group of fragments (1) and the remaining fragments (2) normalized to the KE of all fragments excluding the ones containing only one SPH particle, depending on the wire diameter.

4. Conclusions

Numerical simulations of the experiments [9] on the fragmentation of aluminum projectile with diameter of 6.35 mm on single steel-mesh bumpers of different specific mass were performed in the present work. Specific mass of the mesh bumpers in these experiments was varied by changing the diameter of the wire from which was woven the mesh. The spatial distribution of fragments, their mass and kinetic energy (KE) were determined by the numerical simulations.

The results of the numerical simulations are in good agreement with the experimental data showing that the cloud of fragments composes of two morphologically distinct groups of fragments, which differ greatly in mass: the central group, consisting mainly of four large fragments, and four groups of crosswise arranged and linearly-distributed chains of smaller fragments (Figures 5 and 6). The central group of fragments is formed from material that was entirely concentrated in the rear of the projectile before interaction of the projectile and mesh (Figure 5d).

The numerical simulation (Figure 7) shows that the total KE of the fragments cloud decreases with increasing wire diameter (specific mass) of the mesh. Decreasing the total KE of fragments is associated with a deeper destruction of the projectile. As can be seen from the numerical simulations, the largest fragments (the central group of fragments) in the fragments cloud has the greatest KE, which decreases with increasing the wire diameter (specific mass) of the mesh (Figures 6 and 7). The numerical modeling also shows (Figure 8) that KE of the central group of fragments decreases relative to the total KE of the fragments cloud with increasing the wire diameter (specific mass) of the mesh, while the relative KE of other smaller fragments increases. With regard to the shielding protection of spacecraft from meteoroids and orbital debris clouds, this means a redistribution of KE of fragments over a larger area of the protecting wall, thus reducing the probability of it perforation.

The effect of splitting of the projectile rear may be regarded as an advantage of the steel meshes with corresponding geometrical parameters. The difference between the action of a mesh-bumper combined of three piled meshes $l_a \times d_w = 1.2$ mm $\times 0.32$ mm with total areal density 2.46 kg/m^2 and a single 2.0 mm $\times 0.6$ mm mesh with areal density 1.71 kg/m^2 is demonstrated in Figure 9a,b. The action of piled meshes in Figure 9a is similar to the result that can be obtained on solid thin plate with the same areal density [21], though according some reports [5] the piled meshes may have some advantage under special conditions. This type of bumper, in particular, was studied in [12] as an element of some prototypes of shield protection. The use of a single heavier mesh (Figure 9b) seem to be more favorable owning to the splitting of larger fragments that takes place at lower degree of vacuumization or at normal atmospheric pressure (the same aero-dynamical effect is used in some split-sabot technique). The practical implementation of the splitting effect in deep vacuum requires the use of low-density material to spread the split fragments. The effect of the use of polystyrene foam is presented in Figure 9c that demonstrates the damage on the witness plate made only by the larger fragments. The other elements of the fragments cloud were absorbed by the foam which means that the more balanced distribution of the kinetic energy between the different parts of the fragments cloud can optimize the foam thickness for lower weight. The presented numerical simulation showed that this optimization can be implied, for example, by the correct selection of wire mesh diameter.
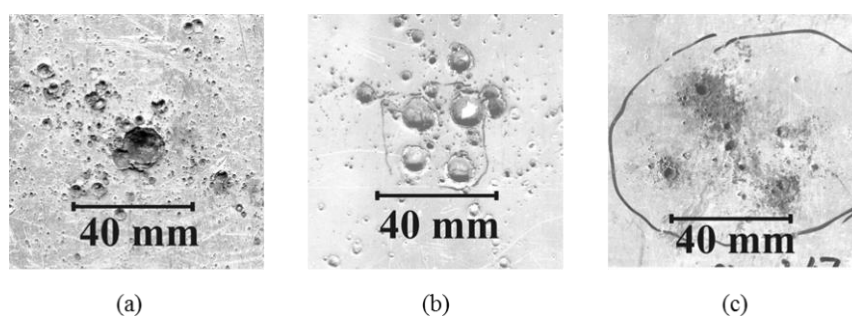
Figure 9. The damage on a witness plate produced by the fragments of 6.35 mm aluminum projectile after impact on a bumper made of: (a) three piled steel meshes $l_a \times d_w$ = 1.2 mm × 0.32 mm with total areal density 2.46 kg/m² at velocity 3.47 km/s, bumper/witness-plate distance 250 mm; (b) a single steel mesh 2.0 mm × 0.6 mm with areal density 1.71 kg/m² at velocity 3.35 km/s, bumper/witness-plate distance was 150 mm at normal atmospheric pressure; (c) a single steel mesh 2.0 mm × 0.6 mm with areal density 1.71 kg/m² at velocity 3.47 km/s, bumper/witness-plate distance 120 mm. A block of polystyrene foam of 80 mm thickness was placed between the mesh and a witness-plate. Mesh/block total areal density was 5.07 kg/m².

Acknowledgments

Conflict of interests

All authors declare no conflicts of interest in this paper.

References

1. Schäfer F, Lambert M, Christiansen E, et al. (2005) The Inter-agency space debris coordination committee (IADC) protection manual. *Proceedings of the 4th European Conference on Space Debris*, 39–44.
2. Christiansen EL, Kerr JH (1993) Mesh double-bumper shield: a low-weight alternative for spacecraft meteoroid and orbital debris protection. *Int J Impact Eng* 14: 169–180.
3. Bezrukov LN, Gadasin IM, Kiselev AI, et al. (2000) About the physical bases of building the protection of the ISS module "Zarya" against impact damage by near-earth space debris fragments. *Cosmonautics Rocket Eng* 18: 140–151 (in Russian).
4. Putzar R, Hupfer J, Aridon G, et al. (2013) Screening tests for enhanced shielding against hypervelocity particle impacts for future unmanned spacecraft. *Proceedings of 6th European Conference on Space Debris*.
5. Horz F, Cintala MJ, Bernhard RP, et al. (1995) Multiple-mesh bumpers: a feasibility study. *Int J Impact Eng* 17: 431–442.

6. Semenov A, Bezrukov L, Malkin A, et al. (2006) Impact fragmentation dependence on geometrical parameter of single mesh bumpers. *Mech Comp Mater Construct* 12: 256–262.

7. Higashide M, Tanaka M, Akahoshi Y, et al. (2006) Hypervelocity impact tests against metallic meshes. *Int J Impact Eng* 33: 335–342.

8. Pang BJ, Lin M, Zhang K (2013) The Characteristics study of debris cloud of the mesh shields under hypervelocity impact. *Proceedings of 6th European Conference on Space Debris*.

9. Shumikhin TA, Myagkov NN, Bezrukov LN (2014) Distribution of kinetic energy among morphologically different parts of debris cloud at high velocity perforation of thin discrete bumpers by compact projectile. *Mech Comp Mater Construct* 20: 319–333 (in Russian).

10. Myagkov NN, Shumikhin TA, Bezrukov LN (2010) Experimental and numerical study of peculiarities at high-velocity interaction between a projectile and discrete bumpers. *Int J Impact Eng* 37: 980–994.

11. Sanchez GA, Christiansen EL (1996) FGB energy block meteoroid and orbital (M/OD) debris shield test report. JSC-27460, NASA Johnson Space Center, Houston.

12. Bezrukov LN, Shumikhin TA, Myagkov NN (2008) Ballistic properties of mesh shielding protection design under high-velocity impact. *Mech Comp Mater Construct* 14: 202–216 (in Russian).

13. Bezrukov LN, Gadasin IM, Shumikhin TA, et al. (2014) The testing of some prototypes of space debris shield protection. *Mech Comp Mater Construct* 20: 646–662 (in Russian).

14. Swift HF (1982) Hypervelocity impact mechanics, In: Zukas JA, Nicholas T, Swift HF, et al., *Impact Dynamics*, New York: John Wiley and Sons.

15. Hallquist JO (2007) *LS-DYNA Keyword User's Manual*, Version 971, Livermore Software Technology Corporation.

16. Monaghan JJ (2005) Smoothed particle hydrodynamics. *Rep Prog Phys* 68: 1703–1759.

17. Myagkov NN, Stepanov VV (2014) On projectile fragmentation at high-velocity perforation of a thin bumper. *Physica A* 410: 120–130.

18. Zel'dovich YB, Raizer YP (1966) *Physics of Shock Waves and High-Temperature Hydrodynamic Phenomena*. New York: Academic.

19. Johnson GR (1983) A constitutive model and data for metals subjected to large strains, high strain rates and high temperatures. *Proceedings of the 7th International Symposium on Ballistics*, 541–547.

20. Kanel GI, Razorenov SV, Fortov VE, et al. (2004) *Shock-Wave Phenomena and the Properties of Condensed Matter*, New York: Springer-Verlag.

21. Piekutowski AJ (1995) Fragmentation of a sphere initiated by hypervelocity impact with a thin sheet. *Int J Impact Eng* 17: 627–638.